Abstract

As important determinants of urban thermal environment, surface roughness and morphology have been extensively studied for sustainable urban development. In this study, we quantify the effect of urban roughness and morphology on the surface urban heat island (SUHI) intensity and its spatiotemporal patterns, over seventeen major cities in six urban agglomerations of China. We employ multisource dataset and derive multiple measures, representative of the roughness and horizontal/vertical indicators of urban morphology. The results show that the correlation between the SUHI intensity and urban morphological indices is significantly strengthened with the heat island intensity, manifested by the contrasting Pearson's r in summer ($r = 0.59 \pm 0.13$) and winter (0.11 ± 0.35). In general, the impact assessed using different measures of surface morphology is consistent on the SUHI intensity, while the one-dimensional (1D) roughness emerges as an adequate index not inferior to more complex morphological parameters. Our study also shows that the impact of urban morphology varies in different geographic and climatic regions, as well as with different urban management, which highlights the importance of locality and site-specific design in implementing effective urban heat mitigation strategies.

Keywords

Land surface temperature; Spatiotemporal patterns; Surface roughness; Urban heat island; Urban morphology

1. Introduction

As a pronounced environmental phenomenon induced by human activities, urban heat island (UHI) is depicted as that urban cores are usually warmer than their surrounding rural areas (Oke 1973). The historical documentation of UHI effect has been very long, dating back to in London as early as 1800s (Howard, 1833). In the past few decades, the effect, mechanisms, and consequence of UHI have extensively studied, based on in situ and remotely sensed measurements, as well as numerical simulations (Arnfield, 2003; Wang, 2022). Depending on the elevation at which ambient temperature is measured, UHI can be further classified into subsurface, surface, canopy, or boundary-layer urban heat island (Oke, 1976; Voogt & Oke, 2003; Mirzaei and Haghighat, 2010). More specifically, the surface urban heat island (SUHI) measured by the land surface (skin) temperature (LST) is a widely used indicator and particularly suitable for remotely sensed data product (Yuan & Bauer, 2007). The peculiarity of urban thermal environment, UHI in particular, induces various and compound impact over the built terrains, including but not limited to, e.g. air quality, energy-water-climate repercussions, and diverse ecosystem services (Howells et al., 2013; Antognelli et al., 2016; Martinez-Bravo et al., 2019; Wang, 2021; Zhang et al., 2022). Today, with over half of the world's population living in urban areas (UN, 2019) and global climate change becoming more prominent (IPCC 2014), it is of crucial importance to further our understanding of UHI to inform policy makers and urban planners more sustainable solutions to urban heat-related issues.

The formation of UHI involves complex interplays of multiple contributors that can be broadly classified as: (1) the use of engineered (mostly impervious) materials (e.g. asphalt, concrete, bricks, etc.) that introduces changes of land surface hydrothermal properties conducive to higher surface temperatures and sensible heat (Arnfield, 2003; Yang et al., 2016), (2)

modified physics of urban flows and turbulent transport (Fernando, 2010; Song & Wang, 2016), (3) changes of radiative heat exchange processes in urban canopies (Wang, 2014a), (4) the reduction of natural (especially vegetated) landscape that suppresses cooling by evapotranspiration (Bowler et al., 2010), and (5) concentrated and enhanced release of waste heat and greenhouse gases, in particular carbon dioxide, attributable to anthropogenic activities (Hutyra et al., 2014; Song et al., 2017; Li & Wang, 2020). Among these factors, land surface roughness and urban morphology received growing recognition in recent years (Li et al., 2011; Peng et al., 2016; Li et al., 2021; Yang et al., 2021; Li et al., 2022). The artificially modified land surface roughness and/or urban morphology can significantly influence the LST by changing the physics of flow in the urban canopy layer, which in turn modifies the turbulent transport of latent and sensible heat fluxes (Wang et al., 2011, 2013). More specifically, a high surface roughness can enhance the surface stress of water vapor and diminish wind speed, while a low surface roughness height has an opposite effect (Sud et al., 1988). Some prior studies indicated that land surface roughness also affect the efficiency of atmospheric heat convection, which in turn modifies the UHI intensity (Lee et al., 2011; Zhao et al., 2014).

To measure land surface roughness and urban morphology, micrometeorological and morphometric methods were employed in prior studies, the former using field observation and the latter using remote sensing dataset (Yang and Friedl, 2003; Tian et al., 2011; Equere et al., 2020). Mechanistically, the surface roughness is usually represented by two aerodynamic parameters, viz. the zero-displacement height (d) and the surface roughness length (z_0). The parameter d represents the adjustments of land surface profiles due to the presence of large obstacles such as buildings and vegetation canopies, while z_0 measures the height above d where the mean velocity of wind in the vertical direction is zero due to substrate roughness (Brutsaert

1982; Jasinski and Crago 1999; Meier et al. 2022). On the other hand, the urban morphology can be portrayed by different aspect ratios of street canyons, such as frontal or roof area factions in typical street canyons (Grimmond and Oke, 1999; Raupach, 1994).

Mounting evidence shows that urban land surface roughness and morphology are among the major driving factors of UHI. Model simulations found that the UHI intensity correlates with the street canyon ratio in a logarithmic function, while the mean UHI intensity could vary as much as 3.0 °C in response to the change in surface roughness and morphology (Zhao et al., 2014; Li et al, 2020). Real-world studies in several cities further demonstrated that the distribution, density and height of building groups have noticeable effects on UHI (Lu et al. 2021; Peng et al. 2018). Among them, the building coverage ratio was found as the most influential factor for LST changes in Hangzhou and Dalian (Yuan et al. 2021; Yang et al., 2021). In comparison, the building density has a seasonally stable positive relationship with LST, which leads to a LST variability as much as 3.6 °C in Wuhan (Li et al. 2021); while another case study of Beijing found that the increase of building compactness related to 1 – 2 °C temperature difference in community scale (Li et al., 2022). Nevertheless, most existing studies were mainly focused on single cities, whereas inter-regional comparisons and spatiotemporal variability remain largely missing. To better leverage the strategies and solutions of urban heat mitigation, policy makers and stakeholders need more site-specific knowledge to support locality-based urban planning (Wang, 2021). For example, in addressing questions like “how to determine the ideal locations of high-rise buildings in a city”, or “what is the suitable distance among building arrays”, answers vary by geographic regions and climate zones. Hence it is imperative to understand how the background climate affects the relationship between urban roughness and

morphology and UHI, or is the relationship homogeneous across different regions, which amounts the main objective of the current study.

In this study, we investigate the influence of urban roughness and morphology on UHI and its spatiotemporal variability by employing remote sensing and urban landscape data in seventeen major cities from six megaregions in China during 2013 – 2017. We aim to reveal the spatiotemporal patterns and, more importantly, potential underlying mechanisms regulating the impact of urban morphology on UHI. In particular, we derive the UHI intensity of selected cities from different background climates from remotely sensed LST data and retrieve the urban surface roughness and morphological indicators using morphometric methods.

2. Data and study area

2.1 Datasets

In this study, we used a portfolio of remote sensing and urban landscape datasets to explore how surface roughness and morphology influence UHI, as summarized in Table 1. The Moderate Resolution Imaging Spectroradiometer (MODIS) onboard Terra and Aqua satellites are widely used due to their capacity to provide long-term, high frequency and wide coverage earth observation data (Wan, 2014). In this study, we used both the daytime and nighttime scenes from MOD11A2 and MYD11A2 datasets of MODIS land products to retrieve LSTs. To avoid the contamination of clouds and possible outliers caused by data processes, all the available 8-day 1-km resolution LST images in the study areas from 2013 to 2017 were composited to yield monthly mean LST images. In addition, the MCD12Q1 dataset of MODIS land products and Landsat 8 multispectral images were employed to determine the urban and rural areas which are critical in UHI studies. MCD12Q1 provides annually 500 m resolution land cover information

according to several land cover classification standards, with the IGBP classification standard adopted in this study (Sulla-Menashe and Friedl, 2018). In comparison, the 16-day 30-meter multispectral images from the OLI sensor onboard Landsat 8 satellite provide more accurate information of built-up areas in the selected megaregions, and its multi-bands information can help us identify properties of the land cover (Masek et al., 2020).

In addition to the aforementioned remote sensing data, we also used vectorial building and road distribution datasets to retrieve the information of urban morphology. The building distribution dataset contains the location, outline, and floor number of buildings in build-up areas of hundreds of Chinese major cities, which is collected and published by the Resource and Environment Science Data Center of Chinese Academy of Sciences (https://www.resdc.cn/data.aspx?DATAID=270). The road distribution dataset is obtained from the OpenStreetMap (OSM) project including an online free database of roads and their related amenities worldwide maintained by volunteers, which can be publicly accessed at https://www.OpenStreetMap.org. In particular, urban roads in this database have been categorized into several classes, e.g. motorway, residential and sidewalk, based on their applications and construction. For each road class, a road width is assigned according to the relative national standard and studies (Sun and Li, 2018). For convenience, these vectorial data were transferred to raster data after preprocessing to match with the remotely sensed data.

Table 1. Datasets used in this study

Type	Source	Collection	Resolution	
			Spatial	Temporal
Remote sensing data	MODIS	MOD11A2 MYD11A2	1-km	8-day
		MCD12Q1	500 m	Annual
	Landsat 8	Collection 2	30 m	16-day
Urban landscape data	Resource & Environment Science Data Center		8 m	Irregularly updated
	OpenStreetMap		6 m	

2.2 Study areas

We chose seventeen major cities located in six megaregions of China as our study areas, all these cities are provincial socioeconomic centers and covered broad spatial variability as well as contrast in climate and geographic conditions (Fig. 1). The three megaregions located along the East Coast of China are the Jingjinji, Yangtze River delta, and Pearl River delta megaregions, from north to south respectively. According to the National Bureau of Statistics (http://www.stats.gov.cn/tjsj/), these are the three biggest megaregions in northern, eastern and southern China based on population and economic production in 2020. Beijing, Tianjin and Shijiazhuang in Jingjinji; Hangzhou, Nanjing and Shanghai in Yangtze River delta; Guangzhou, Foshan and Shenzhen in Pearl River delta are selected as study cities. As the build-up area of Guangzhou and Foshan has been overlapped in recent development, it will be studied as one greater Guang-Fo metropolitan in the subsequent analysis. In contrast to the three coastal megaregions, Chengyu is located in the Sichuan Basin; Northwestern is located between Tibetan Plateau and desert in northern China; Northeastern is located in Songnen Plain under mid-temperature humid climate. Eight study cities were chose from these three non-coastal megaregions, including Chengdu, Chongqing, Hohhot, Lanzhou, Yinchuan, Changchun, Harbin and Shenyang.

The seventeen cities cover all major climate zones in China, except the cold-temperate humid in most northern China, tropical humid in most southern China and Plateau arid/semiarid in Tibetan Plateau. Five of the six megaregions are located in monsoon climate, while Northwestern is located in continental arid climate zone zones (Domrös and Peng, 2012). From north to south, the annual mean temperature increases from 5.5 °C in Northeastern to 22.4 °C in Pearl River Delta, while the annual precipitation rate raises from around 500 mm in

Northwestern to over 2000 mm in Pearl River Delta. The wide distribution, high population density, and various climate conditions of the selected areas therefore enables a comprehensive study of the thermal environment in Chinese megacities.

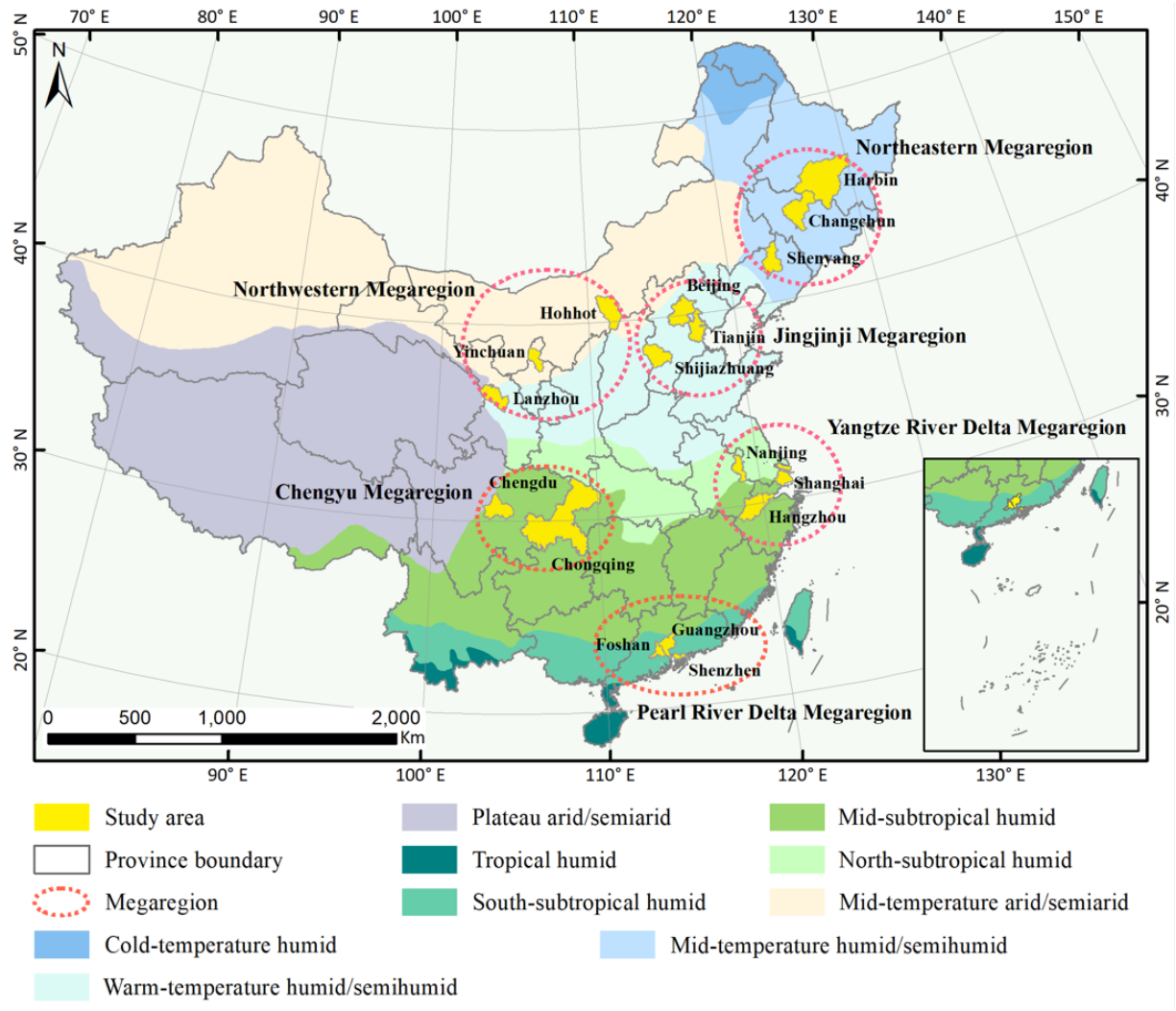

Figure 1. Map of study areas of six Chinese megaregions including Jingjinji, Yangtze River delta, Pearl River delta, Chengyu, Northwestern, and Northeastern megaregion, demarked in red dashed circles, containing seventeen major cities. The background color indicates the classification of climate in different regions.

3. Methods

3.1 SUHI intensity (ΔT)

This study focuses exclusively on the surface UHI effect. While other ambient temperatures, e.g. near-surface air or boundary-layer temperatures are also commonly used UHI indicators (Oke, 1976), the skin temperature of land surface better represents the localized thermal environment. The SUHI intensity is defined as,

$$\Delta T = T_{\text{urban}} - T_{\text{rural}} \quad (1)$$

where T_{urban} and T_{rural} represent the LST of urban and rural areas, respectively, and for brevity, we omit the denotation of "surface" in the temperature variables.

The sampling of corresponding urban and rural areas is of critical importance in the calculation of ΔT, for different standards or thresholds applied to select them could impact the results directly (Chakraborty and Lee, 2019). Considering the rapid urbanization in these cities during the study period, the IGBP land cover classifications from MODIS MCD12Q1 dataset and the Landsat 8 derived Normalized Difference Built-up Index (NDBI) images were adopted to choose the urban and rural areas. The two remotely sensed datasets have relatively high update frequency, which can help us better capture the expansion of urban areas. The various vegetated land types from IGBP (class 1 to class 12) are all defined as natural land surfaces. To avoid the spatial footprint of urban heat, we generated a 10-km wide outer buffer of the study cities' administration boundary, only the natural land surfaces in this buffer are selected as rural areas. The urban areas are derived from the concentrated built-up land type (IGBP class 13) according to the NDBI images (Sulla-Menashe and Friedl, 2018). The NDBI is calculated as:

$$NDBI = (SWIR - NIR) / (SWIR + NIR) \quad (2)$$

where *SWIR* is the short-wave infrared band of Landsat 8 (band 6 and band 7), and *NIR* is the near infrared band of Landsat 8 (band 5) (Zha et al., 2003). The NDBI images were first calculated by the original resolution of corresponding Landsat bands, then resampled to the same resolution of MCD12Q1 dataset for later use. A threshold is set based on the distribution of NDBI to delineate the densely built-up areas in a city and the villages with sparse buildings scattered around it. The intersections of built-up land type from MODIS and densely built-up areas from Landsat within this city's administration boundaries are used as urban samples. The ΔTs of study cities are obtained by the mean LSTs of their urban areas minus the mean LSTs of corresponding rural areas at the same time. ΔTs of pixels of urban areas are retrieved by the pixel's LST value minus the mean LST of corresponding rural areas.

3.2 Urban surface roughness parameters

3.2.1 Urban aerodynamic roughness length

The quantification of the land surface roughness length (z_0) and zero displacement height (d) need comprehensive information about vertical wind profiles and land surface geometry, which is challenging to local field measurements or remote sensing observation (Jasinski and Crago, 1999; Yang and Friedl, 2003). More specifically, the value of surface roughness depends on the height and spacing of the largest objects acting to retard the surface airflow (Schaudt and Dickinson, 2000), which lead researchers to develop multiple algorithms to derive z_0 and d from land surface structure data (Rotach, 1994; Li et al., 2021; Nakai et al., 2008). For forest canopies, z_0 and d are usually expressed as functions of vegetation canopy height (Skamarock et al., 2008; Wang et al., 2013). For example, a classic algorithm proposed by Garratt (1994) uses 1/8 and 2/3 of the mean height of vegetation to parameterize z_0 and d, respectively. Urban areas have

relatively more uniform structures, in contrast to forest canopies where the ratios between the land surface roughness and the canopy height varies with diverse vegetation types. Hence prior studies often derived z_0 and d from urban morphology data (Grimmond and Oke, 1999). Given z_0 is always an order of magnitude smaller than d in urban areas, here we use a lumped urban aerodynamic roughness length (z_{urban}) to combine z_0 and d, defined as the height above the urban land surface when the wind speed becomes zero under neutral conditions, as

$$z_{urban} = h / 3 \quad (3)$$

where h is the mean building group height of this area. The values of z_{urban} were first computed at the building scale and then resized to match the resolution of LST data.

3.2.2 Street canyon aspect ratios

The parameter z_{urban} is only representative of the one-dimensional (1D) urban morphology in the vertical direction (Bottema, 1997). For a more holistic description of the urban morphology, it is common to adopt the measure of street canyon aspect ratios (Raupach, 1994). For urban areas, there are two indices typically used to describe the street canyon parameters: the first one is the frontal-area index, which describes the ratios of the total frontal areas and the total lot areas of building groups, and the second one is the plan-area index, which indicates the ratios of the total plan areas and the total lot areas of building groups (Raupach, 1994; Hagishima et al., 2009). As the resolution of geospatial data improves with the advance of remote sensing technology, both parameters emerge as useful representatives of the land surface roughness for realistic urban topographies with good accuracy (Grimmond and Oke, 1999; Moriwaki et al., 2007).

In the light of prior studies, here we define two indices to represent 2D urban morphology at vertical and horizontal dimensions, respectively. The first one is the vertical aspect ratio (*VAR*) between the building height and canyon width, as

$$VAR = h / w \tag{4}$$

where w is the mean width of the street canyon. The value of *VAR* is indicative of the morphology of street canyon mostly representative at the neighborhood scale, e.g., a large *VAR* value signals a "deep and narrow" street canyon. In addition, we also define a horizontal aspect ratio (*HAR*), analogous to the frontal-area ratio used in previous studies,

$$HAR = A_p / A_r \tag{5}$$

where A_p is the projected area of building groups on the horizontal plane, and A_r the horizontal area of roads in urban gridcell. The ratio *HAR* is representative of the building density in a built environment, with a small *HAR* indicating a sparsely built area. Together with the aforementioned land surface aerodynamic roughness length (1D), these aspect ratios provide a relatively comprehensive descriptions of urban morphology, which are directly or indirectly related to other morphological parameters such as sky view factor.

After obtained the SUHI intensity and urban surface roughness parameters, these data are registered and resampled to 2 × 2 km grid size. The correlations between these parameters were evaluated by Pearson's correlation coefficient:

$$r = \frac{n\sum x_i y_i - \sum x_i \sum y_i}{\sqrt{[n\sum {x_i}^2 - (\sum x_i)^2][n\sum {y_i}^2 - (\sum y_i)^2]}} \tag{6}$$

where r is the correlation coefficient, n is the sample size, and x_i, y_i are the individual samples. Overall, the structure and flowchart of the current study, with the specific dataset and/or methods adopted in each section, are illustrated in Figure 2.

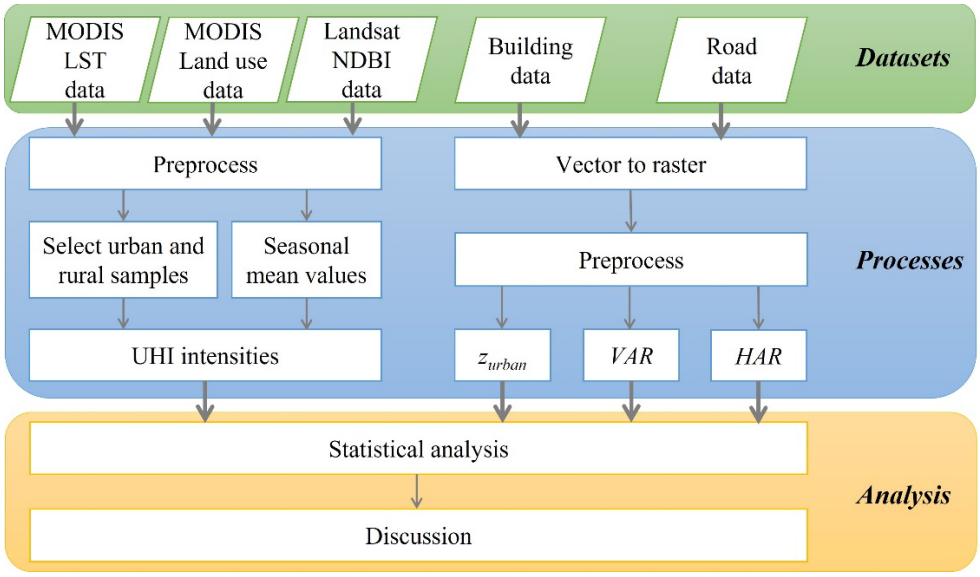

Figure 2. Flow chart of this study, the datasets in Table 1 were preprocessed into same spatiotemporal resolutions and calculated using the methods in Section 3, the results were then analyzed and discussed.

4. Results

4.1 Spatiotemporal variations of SUHI intensities in major Chinese cities

The SHUI intensities of the study cities are shown in Figure 3, where the trends are in general consistent with what reported in prior studies (Peng et al., 2012; Zhou et al., 2014). All the cities have comparative intense SHUI in warm seasons (May to October) than in cold seasons during 2013 – 2017, with the seasonal fluctuations being much stronger in other megaregions than in Pearl River Delta and Northwestern, due to the mild seasonality and artificial irrigation in arid region respectively (Hou et al., 2022). Spatially, two cities from the Chengyu megaregion have the most intensive SUHIs, with the mean values greater than 3 °C in winter and 7 °C in summer, respectively. This could be largely attributed to their mountainous topography that strengthens the urban-rural difference since urban areas are located in plains surrounded by rural areas scattered across mountains (Zhou et al., 2014). Cities from the three northern megaregions

have relatively smaller SUHI intensity and standard deviations, even manifesting urban oasis effect (e.g. during cold seasons in Tianjin and Shenyang) with urban cores cooler than surrounding rural areas. Similar phenomena were also observed in Middle East and North Africa (Peng et al., 2012). This could be attributed to the evaporative cooling caused by planted vegetations and artificial irrigation in urban areas (Guhathakurta et al., 2007; Wang et al., 2018, 2019a, 2019b), which is more outstanding under the arid/semiarid climate in northern China. Besides, as the croplands are contained in the rural areas, the crop phenology induced by artificial cultivation tends to exaggerate the SUHI intensity because of the deviation of urban/rural green trends. The discrepancy of the crops and farming seasons also contribute to the variations of the spatiotemporal patterns of the SUHI intensity in these cities.

Besides the commonly presented inverted-U shape for the annual distributions of the SUHI intensity, an interesting finding often ignored is the seasonal (sub-annual) V curve happens in many cities (Fig. 3), e.g. spring in Shijiazhuang and Lanzhou or early summer in Nanjing and Shanghai. Diverse factors could contribute to form this pattern. In Shijiazhuang and Lanzhou, it is likely due to the seasonal hysteresis of SUHI intensity caused by artificial irrigation (Sun et al., 2013; Wang, 2014b; Manoli et al., 2020). In Southeast China, i.e. Nanjing and Shanghai, the occurrence of seasonal V curves could be attributed to the contamination of the remotely sensed data by cloud covers, which is much more significant during rainy seasons in Yangtze River Basin and affects the accuracy of the derived LST.

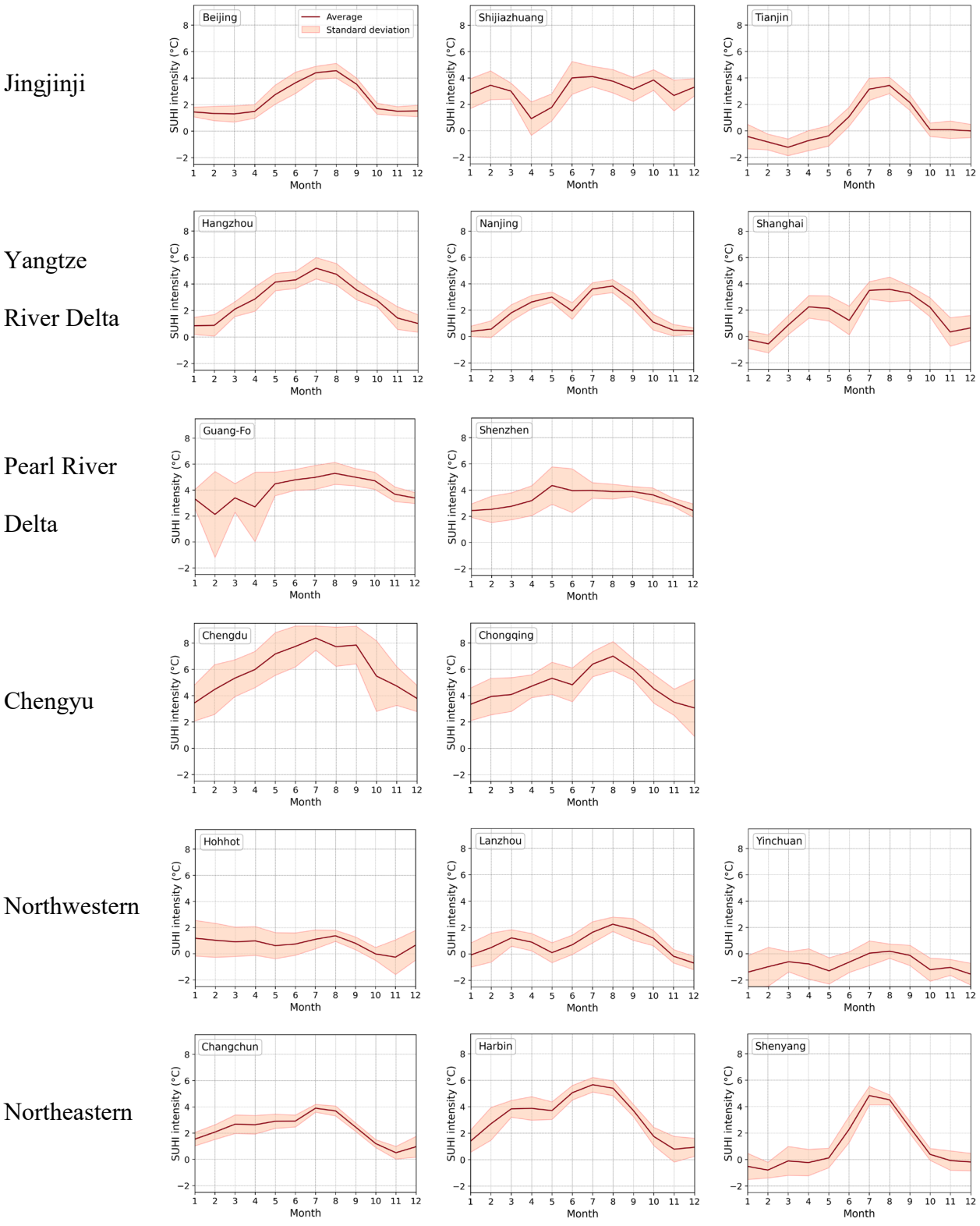

Figure 3. Spatiotemporal variations of the monthly average SUHI intensities of seventeen major cities of six megaregions in China.

4.2 Statistical distributions of urban morphological parameters

The violin plots in Fig. 4 show the statistics of three urban surface roughness parameters, viz. z_{urban}, *VAR*, and *HAR*, in the selected cities. The width of each cluster represents the number of the 2 × 2 km grids in each city, and the box plots in the middle of the clusters show the mean values and quantiles of the three parameters of the cities. As shown in Fig. 4 (a), the values of z_{urban} of most cities are concentrated between 0 – 1 m, at least half of the gridcells in all the cities have z_{urban} values lower than 1 m. The largest value of z_{urban} is over 4 m and appears in Guang-Fo, while the highest mean z_{urban} is found in Tianjin. The statistical distributions of *VAR* of the study cities are similar to those of z_{urban} (Fig. 4b), despite over half of the gridcells in seven cities, including Beijing, Shijiazhuang, Shanghai, Hohhot, Yinchuan, Changchun and Harbin, are larger than 1 with Shijiazhuang has the largest value (> 5). Moreover, Shenyang has the highest value of *HAR*, while nearly 75% of grid values of *HAR* in Tianjin are over 2 when grided values of *HAR* in most cities are concentrated between 0 – 2. The violin shape of the statistical distributions of these parameters is global, showing that the prevailing built structure in most Chinese cities mainly consists of regular multistorey buildings and a small fraction of high-rise buildings.

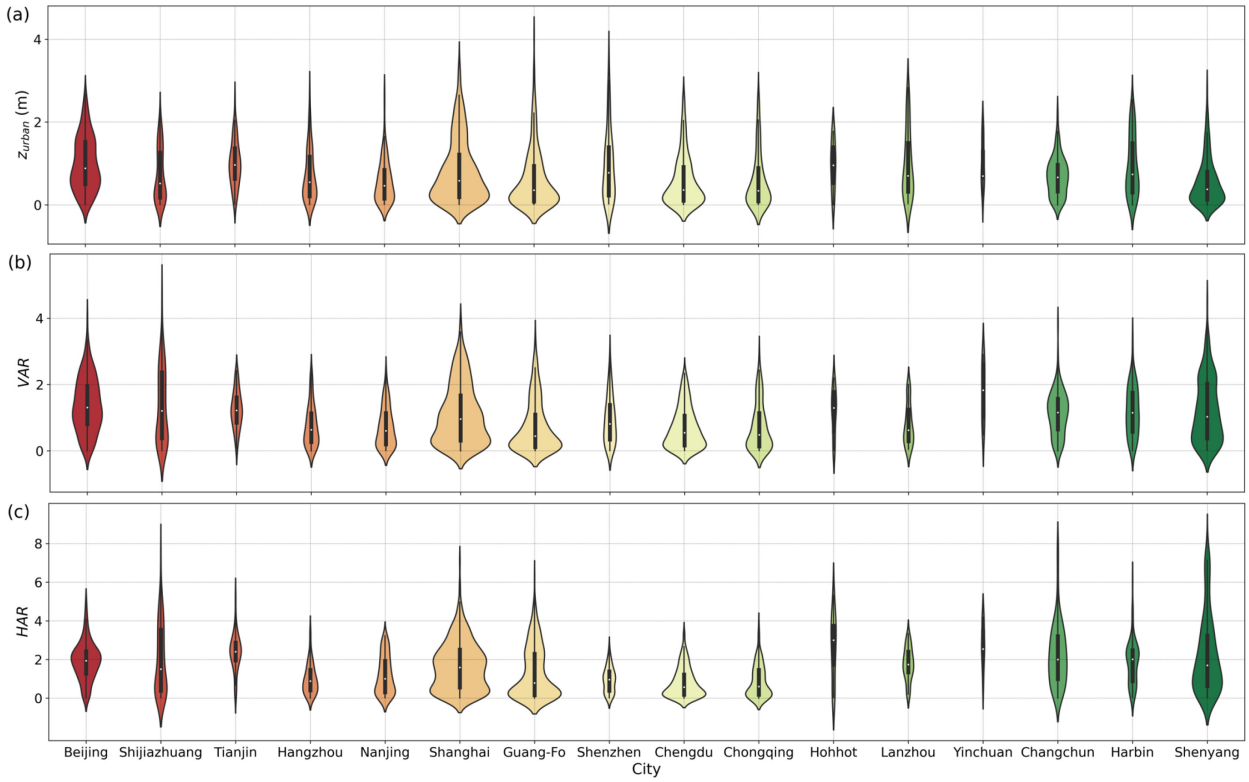

Figure 4. Statistics of (a) z_{urban}, (b) *VAR*, and (c) *HAR* of seventeen major cities in China, the violin shapes show the frequency distributions of the parameters of these cities and the box plots in the center of the violins show the quantiles of the parameters with white dots indicating the median.

4.3 Relationships between the SUHI intensity and urban morphology

After statistical characterizing the SUHI intensity and the representative urban morphological parameters above, we then proceed to quantify their correlation in this section. The results are shown in Figures 5 to 10, where the subplots for the same city are grouped in the row while columns are grouped by morphological parameters. It is clear that the three parameters have significant positive relationships with SUHI intensity in all the study cities (annual mean and standard error of r is 0.37 ± 0.30), despite their spatiotemporal variabilities. While z_{urban},

VAR and *HAR* are representative of different aspect of urban morphology, i.e. building height, canyon geometry, and building density, respectively, their correlations with the SUHI intensity are strikingly similar (0.35 ± 0.34, 0.35 ± 0.31 and 0.41 ± 0.26 for *r* values of z_{urban}, *VAR* and *HAR* respectively). In general, the SUHI intensity increased with morphological parameters, the correlation appears strongest in summers with highest seasonal mean *r* values (0.59 ± 0.13) in all the study cities, followed by autumns and springs. The *r* values in winter are small (0.11 ± 0.35), or even reversed to be negative in Jingjinji and Northwestern megaregions (−0.22 ± 0.36 and −0.19 ± 0.32), indicating the often-weak relationship between the SUHI intensity and urban morphology in cold seasons.

Given the different background climates of the six megaregions, the correlation between these parameters and the SUHI intensity has manifest spatial variability. The mean and standard error of *r* in Jingjinji, Yangtze River Delta, Pearl River Delta, Chengyu, Northwestern and Northeastern megaregions are 0.31 ± 0.42, 0.48 ± 0.18, 0.47 ± 0.19, 0.36 ± 0.11, 0.22 ± 0.41 and 0.44 ± 0.22 respectively. In Jingjinji, the scatters are gathered into four rather distinctive clusters corresponding to four seasons (Fig. 5). In contrast, the scatters of spring and autumn in Yangtze River Delta and Chengyu are blended into one cluster (Figs. 6 and 7). Moreover, the scatters of all four seasons in Pearl River Delta do not differentiate significant from one another (Fig. 8), indicating weak seasonality in the region largely due to the prevailing hot and humid subtropical climate. The distributions of the scatters in Northwestern and Northeastern are similar to Jingjinji, despite the urban sizes in Northwestern are significantly smaller than that of Jingjinji and Northeastern, demonstrating the effect of seasonality in mid-temperature regions. Overall, the seasonal variability of correlation between the SUHI intensity and urban morphological

parameters decreases from North to South China, clearly suggesting the heterogeneous impact of the background climate on local urban thermal environment.

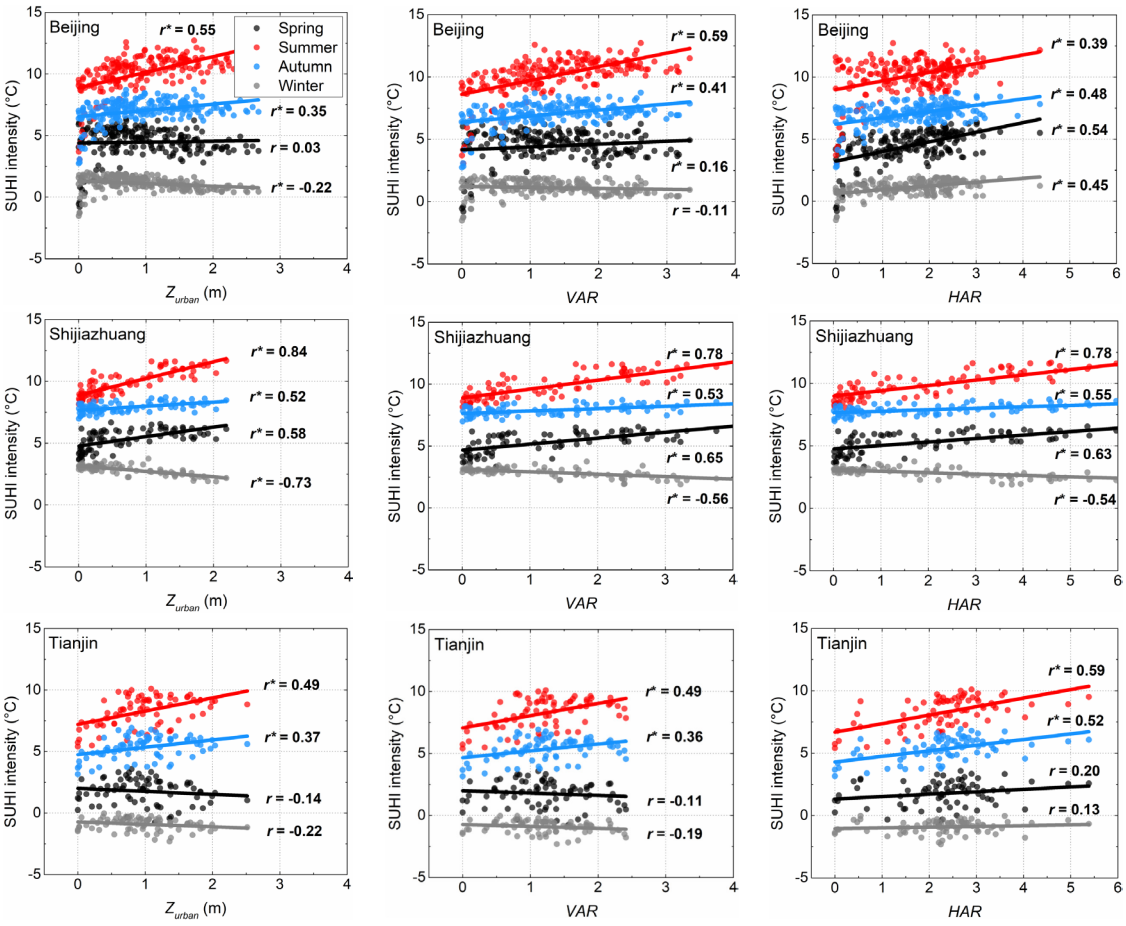

Figure 5. The statistical correlation between the SUHI intensity and urban morphological parameters of three cities in Jingjinji megaregion; *r* is the Pearson correlation coefficient, and * stands for *r* value passing the 0.95 confidence level.

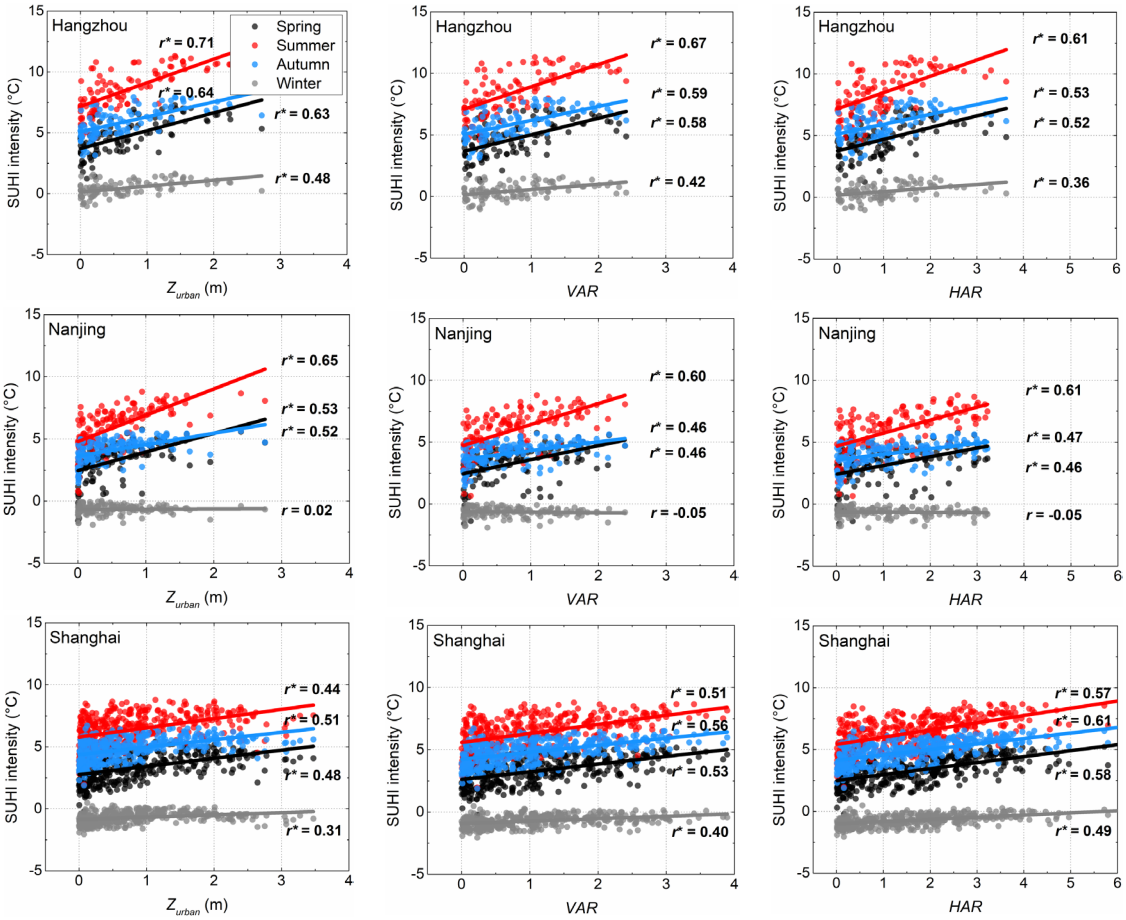

Figure 6. Same as Fig. 5, but for three cities in Yangtze River Delta megaregion.

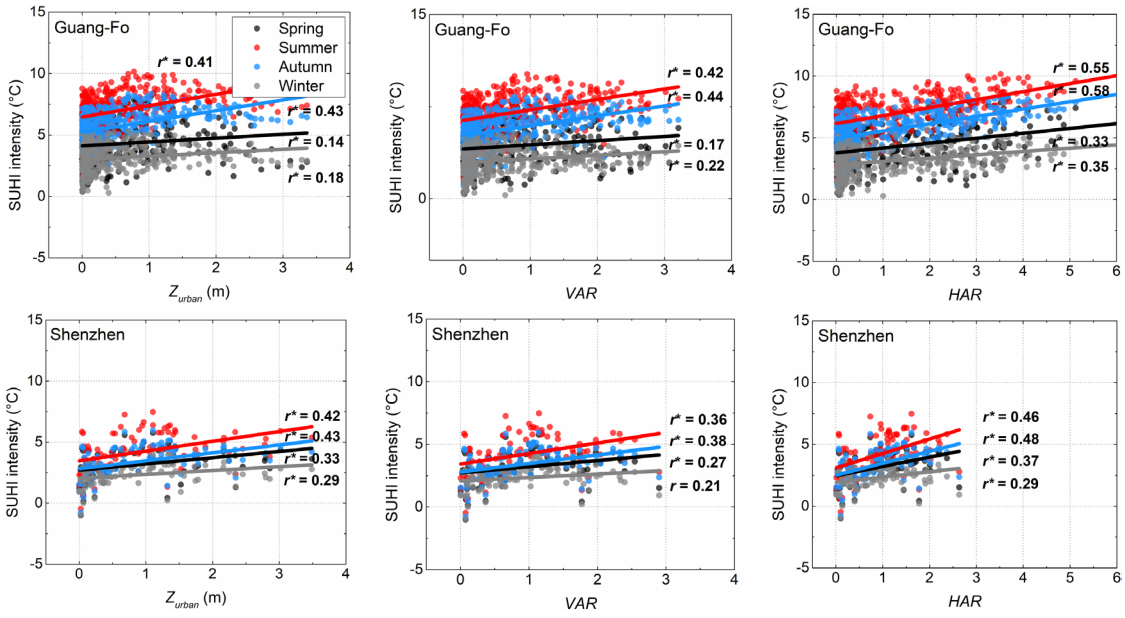

Figure 7. Same as Fig. 5, but for three cities in Peral River Delta megaregion.

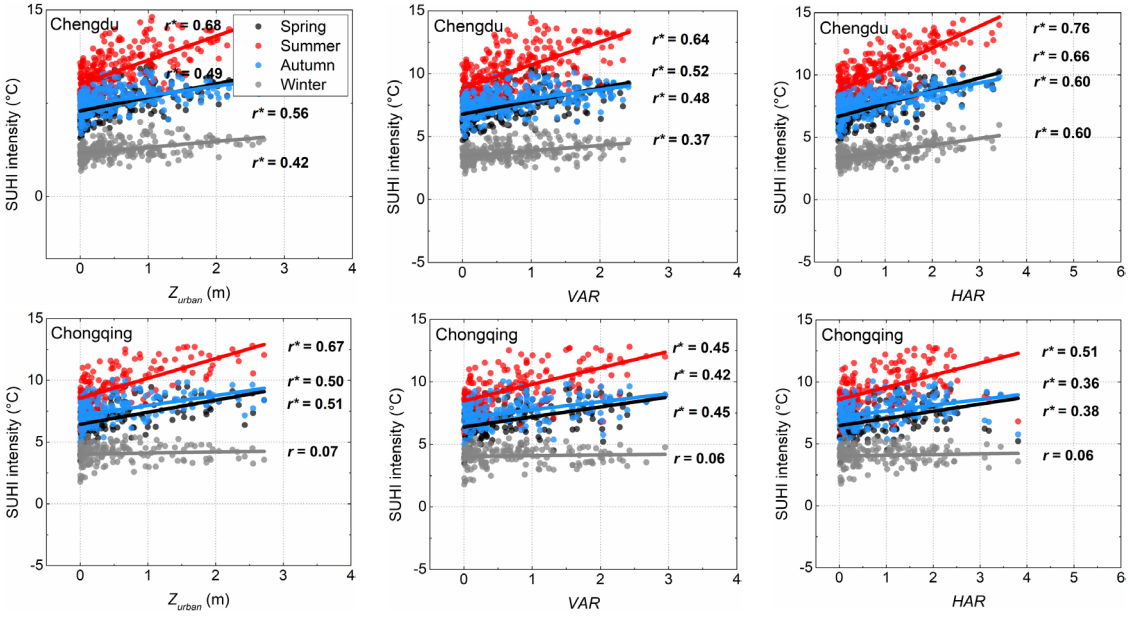

Figure 8. Same as Fig. 5, but for two cities in Chengyu megaregion.

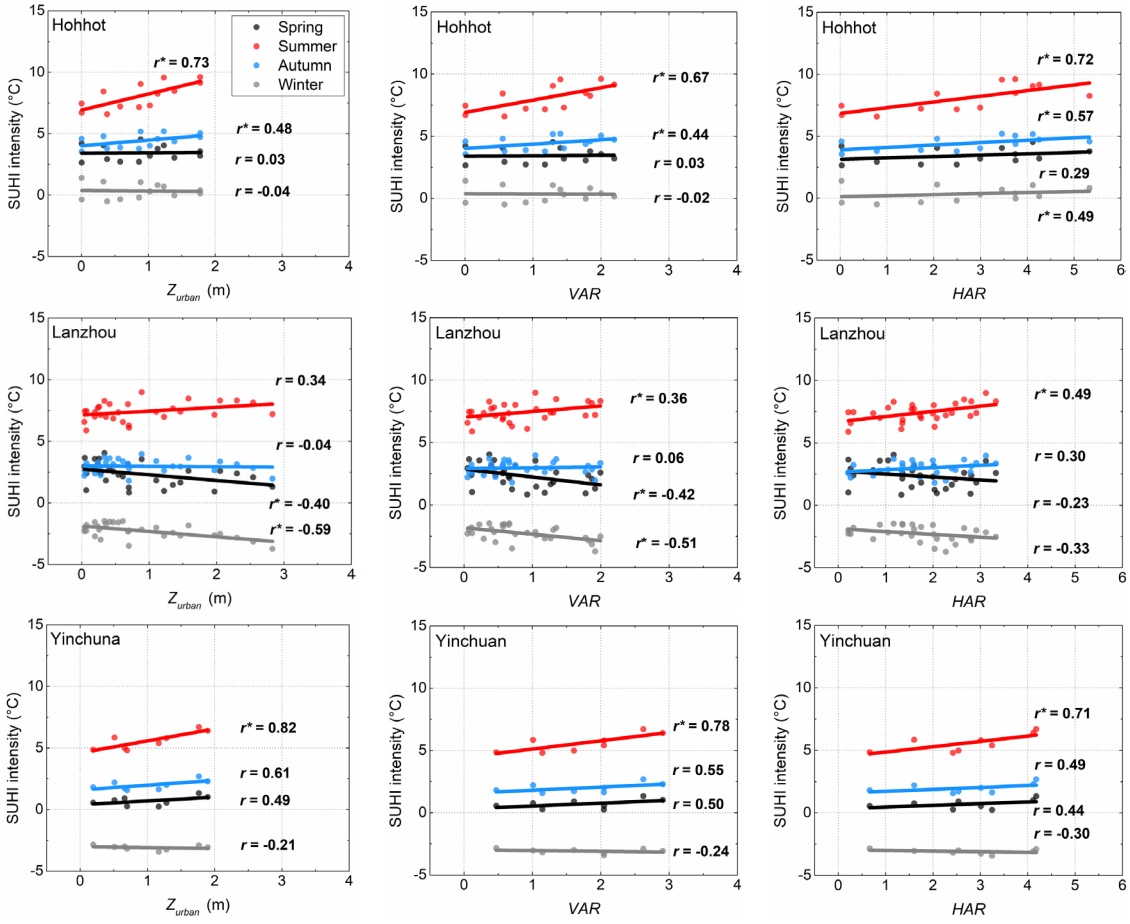

Figure 9. Same as Fig. 5, but for three cities in Northwestern megaregion.

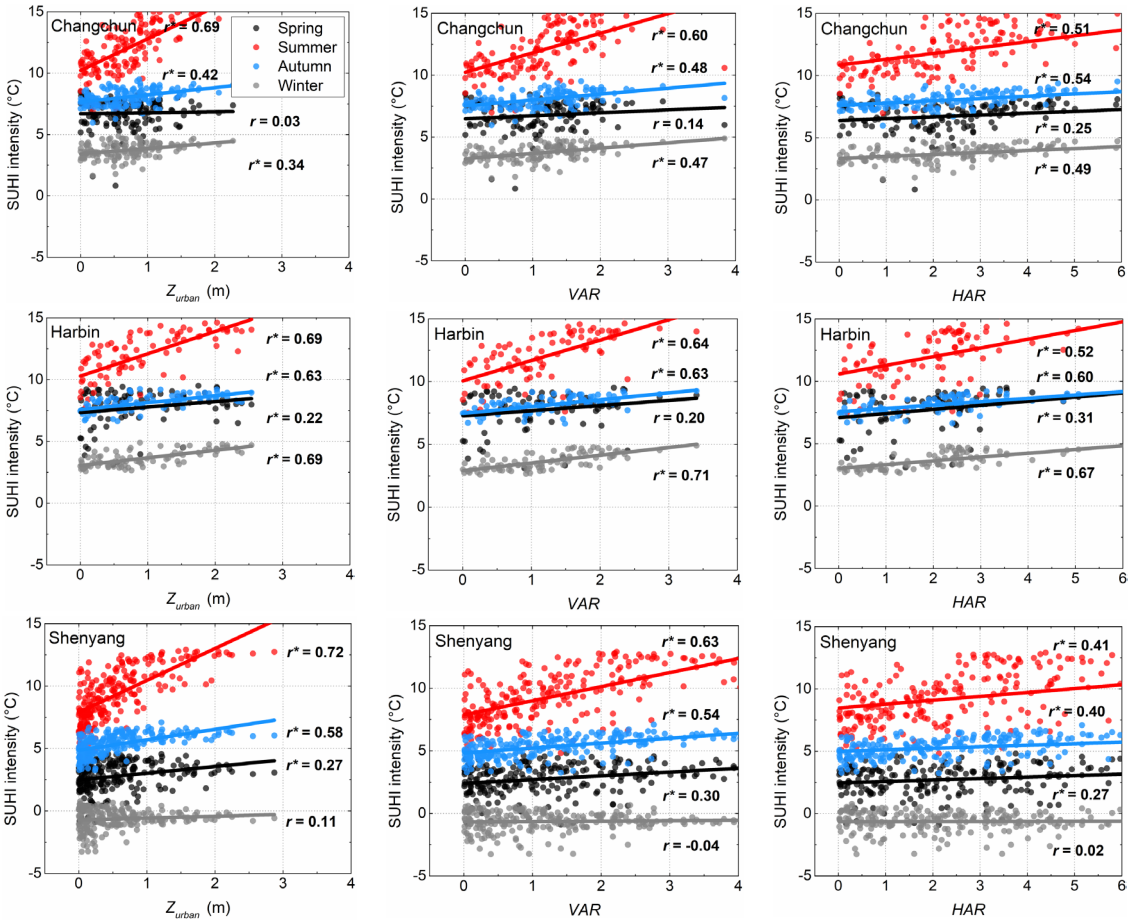

Figure 10. Same as Fig. 5, but for three cities in Northeastern8 megaregion.

5. Discussion

As a critical determinant of the UHI effect, land surface roughness and morphology have been extensively studied in the literature (Lee et al. 2011; Li et al. 2020; Myint et al. 2017). Overall, the results of this study are consistent with that of prior studies, revealing that the SUHI intensity has a positive relationship with the spatial distribution and density of buildings (Guan et al., 2021; Peng et al., 2018). The left columns of Figs. 5 to 10 show the relationships between the SUHI intensity and the urban roughness z_{urban} proportional to building height. The same correlation was qualitatively observed and reported in case studies of Wuhan and Hangzhou (Li et al., 2021; Lu et al., 2021). With respect to the 2D morphological parameters, previous case

studies reported the building coverage/area (*HAR*) is the dominant factor of SUHI variability (Li et al., 2021; Lu et al., 2021; Yuan et al., 2021). Nevertheless, the current study finds that the influence of *VAR* on SUHI is comparable to that of *HAR* (middle and right columns from Figs. 5 to 8). Furthermore, the correlation between the SUHI intensity and *VAR* or *HAR* exhibits nearly identical seasonal fluctuations.

It is noteworthy that numerical simulations of urban climate found that the LST in a street canyon bears nonlinear relationship with the building-height-to-canyon-width ratio, viz. *VAR*, arising from the complex interplay of radiative shading and trapping effect by the presence of building structure (Song & Wang, 2015, 2016). As a consequence, the correlation between SUHI and *VAR* is expected to be nonlinear, provided that the variation of *VAR* covers a broad enough range, say 0.1 – 10. In this study, however, we only find the increasing trend of SUHI intensity with *VAR*. This is mainly due to that the prevailing building type in most Chinese cities renders a relatively narrow range of *VAR* (mostly less than 3, see Fig. 4). Nevertheless, it is caveated that in sufficiently densely built areas (e.g. downtown or commercial district teeming with skyscrapers) the simple linear correlation between *VAR* and the SUHI intensity may break down, and more sophisticated technique (e.g. machine learning, see Li et al., 2022) is needed to quantify their relationship, as well as for optimal urban design.

When referring back to Fig. 3, the SUHI intensity of eleven Chinese cities have coherent trends but each varies individually, suggesting diverse mechanisms (as described in the Introduction) synergistically determines the urban thermal environment. Among these determinants, urban morphology is responsible for a part of, albeit critical, SUHI variability and its spatiotemporal patterns. In addition to urban morphology, prior studies also suggest that the background climate and evapotranspiration of vegetation are the major factors that influence

urban thermal environment (Zhao et al., 2014). Seasonal changes in background temperature have a significant impact on spatial distributions of SUHI intensity, the intensive shortwave radiation during summertime not only heats the near-surface atmosphere, but also accelerates the speed of heat release from artificial structures in urban areas (Zhou et al., 2014), further amplify the difference of heat storage and convection ability between urban and rural areas and lead to strong SUHI (Hou et al., 2022). At the same time, as the vegetation coverage in Northern China mainly consists of temperate broad-leaf forests, the evaporative cooling by plants in summers also exaggerates the temperature difference between vegetated and impervious land surfaces (Peng et al., 2012), another way to intensify UHI.

Furthermore, other contributing factors to urban thermal environment can also be significant, one being the topography of cities. For example, the SUHI intensity of Chengdu and Chongqing (Fig. 3) show that cities built over mountainous terrains can exhibit stronger SUHI intensity, even compared to cities more densely built or populated. This can be attributed to the drastic changes in land cover and/or altitude in mountainous areas (Hou et al., 2022; Zhou et al., 2014). In addition, anthropogenic activities, such as urban irrigation, plays an increasingly important in regulating the thermal environment in cities (Wang et al., 2019a). It has been found that irrigation changes the rate of soil water convection, which in turn lead to the hysteresis effect of LST evolution (Wang, 2014b). This seasonal hysteresis due to irrigation is likely responsible to the anomalous SUHI variation in Shijiazhuang and Tianjin (Fig. 3) during springs and early summers, which accelerates the vegetation growth, leading to a higher evapotranspiration cooling effect than in rural areas and forming a temporary urban heat oasis (Zhao et al., 2016; Zhou et al., 2013).

Despite the spatiotemporal variability in the four megaregions, the strongest correlation to morphological parameters (both r and slope of regression functions) always appears in summer while the weakest appears in winter. Spatially, the seasonal differentiation of this correlation decreases from North to South, due to the variation of background climate conditions. From the warm-temperature humid climate zone (Jingjinji megaregion) to the mid- (Yangtze River Delta and Chengyu megaregions) to south-subtropical humid climate zone (Peral River Delta megaregion), the seasonal fluctuations of temperature and precipitation become gradually milder (Domrös and Peng, 2012), contributing to the distinctive or insignificant seasonality in Fig. 5 and Fig. 8, respectively.

The temporal differentiations of these relationships, on the other hand, reveal more detailed mechanisms for formation of UHI. The correlation between urban morphology and the SUHI intensity is weakest in winter (Figs. 5 to 10), even becomes negative (Figs. 5 and 9). In the winter of Jingjinji and Northwestern megaregion, contrary to the common belief that the UHI intensity increases with building density (Guan et al. 2021; Lu et al., 2021), it can decline with all three urban roughness and morphology indicators. This is because that the presence of high-rise buildings in urban cores, in conjunction with the low zenith angles of the sun in winter in northern China, can effectively impede the solar radiation incident on street canyon facets, and effect known as radiative shading (Song & Wang, 2015; Li et al., 2021).

6. Concluding Remarks

In this study, we quantified the spatiotemporal patterns of the relationship between urban morphology and the SUHI intensity in major Chinese cities, using MODIS LST data and urban landscape data during the 2013 – 2017 period. In general, it is found the SUHI intensity is

positively correlated with the surface roughness (z_{urban}), canyon geometry (*VAR*), as well as building density (*HAR*). in addition, the spatiotemporal variation of this correlation is strongly regulated by the seasonality and background climate in the study regions. In particular, when the SUHI intensity rises with background temperatures, its dependence on the urban morphology also becomes more significant, as revealed by the increase in values of both *r* and slope of regression. In megaregions that have notable seasonality, these relationships always achieve their highest degree in summer (mean and standard error of *r* is 0.59 ± 0.13) and lowest degree in winter (0.11 ± 0.35). Furthermore, most parameters have negative relationships with the SUHI intensity in the winter of Jingjinji and Northwestern megaregions (-0.22 ± 0.36 and -0.19 ± 0.32), implying the effect exerted by urban surface roughness and morphology is not unidirectional, and could contribute to urban oasis either.

Moreover, the intercomparison among the three urban morphological parameters show that their influence on the urban thermal environmental are comparable, despite the parameters are calculated in different dimensions. While the 1D surface roughness z_{urban}, as a function of building height alone, appears to be a simplified measure of urban morphology, it turns out to be good representative of the 2D urban geometry and building density as well. This makes physical sense as in real urban planning, all three parameters are highly dependent, e.g. a built environment teeming with high-rise buildings (like the commercial districts in the Jingjinji megaregion or downtown Manhattan) will feature high surface roughness z_{urban}, deep and narrow street canyon (large *VAR*), and high building density (large *HAR*) at the same time.

It is caveated that urban morphology is only a partial, albeit important factor, contributing to regulate the thermal environment in cities. Nevertheless, the findings of this study enhance our understanding of how urban morphology affects UHI, and more importantly, how building

structures can be strategically planned to counteract the heat island effect. One particular example is the potential nonlinearity of the correlation between the SUHI intensity and the street canyon geometry (*VAR*), and other morphological parameters as well, due to complex interactions of radiative trapping and shading effect in street canyons. The threshold *VAR* of this nonlinearity can be utilized in planning for future cities, especially under the stress of intensification of urban cores. Strategical urban planning as such will require more sophisticated tools such as multiscale urban climate simulations and/or machine learning based surrogate modeling or optimization.

Acknowledgements

This study is supported by the National Science Foundation (NSF) under Grant No. AGS-1930629 and CBET-2028868, the National Aeronautics and Space Administrations (NASA) under grant No. 80NSSC20K1263, and the National Natural Science Foundation of China under grand No. 41971315. H. Hou also acknowledges the support from the University of Chinese Academy of Sciences Joint Ph.D. Training Program.

References

Antognelli, S., &Vizzari, M. (2016). Ecosystem and urban services for landscape liveability: A model for quantification of stakeholders' perceived importance. Land Use Policy, 50, 277-292.

Arnfield, A.J. (2003). Two decades of urban climate research: a review of turbulence, exchanges of energy and water, and the urban heat island. International Journal of Climatology, 23, 1-26

Bottema, M. (1997). Urban roughness modelling in relation to pollutant dispersion. Atmospheric Environment, 31, 3059-3075

Bowler, D.E., Buyung-Ali, L., Knight, T.M., & Pullin, A.S. (2010). Urban greening to cool towns and cities: A systematic review of the empirical evidence. Landscape and Urban Planning, 97(3), 147-155.

Brutsaert, W. (1982). Evaporation into the atmosphere: theory, history and applications. Springer Science & Business Media

Chakraborty, T., & Lee, X. (2019). A simplified urban-extent algorithm to characterize surface urban heat islands on a global scale and examine vegetation control on their spatiotemporal variability. International Journal of Applied Earth Observation and Geoinformation, 74, 269-280

Domrös, M., & Peng, G. (2012). The climate of China. Springer Science & Business Media

Equere, V., Mirzaei, P. A., & Riffat, S. (2020). Definition of a new morphological parameter to improve prediction of urban heat island. Sustainable Cities and Society, 56, 102021

Garratt, J.R. (1994). The atmospheric boundary layer. Earth-Science Reviews, 37, 89-134

Guhathakurta, S., & Gober, P. (2007). The impact of the Phoenix urban heat island on residential

water use. Journal of the American Planning Association, 73(3), 317-329

Grimmond, C., & Oke, T.R. (1999). Aerodynamic properties of urban areas derived from analysis of surface form. Journal of Applied Meteorology and Climatology, 38, 1262-1292

Guan, Q., Yao, Y., Ma, T., Hong, Y., Bie, Y., & Lyu, J. (2021). Under the Dome: A 3D Urban Texture Model and Its Relationship with Urban Land Surface Temperature. Annals of the American Association of Geographers, 112, 1369-1389

Hagishima, A., Tanimoto, J., Nagayama, K., & Meno, S. (2009). Aerodynamic Parameters of Regular Arrays of Rectangular Blocks with Various Geometries. Boundary-Layer Meteorology, 132, 315-337

Hou, H., Su, H., Liu, K., Li, X., Chen, S., Wang, W., & Lin, J. (2022). Driving forces of UHI changes in China's major cities from the perspective of land surface energy balance. Science of the Total Environment, 829, 154710

Howard, L. (1833), The climate of London deduced from meteorological observationsRep., Harvey and Darton, London.

Howells, M., Hermann, S., Welsch, M., Bazilian, M., Segerstrom, R., Alfstad, T., et al. (2013). Integrated analysis of climate change, land-use, energy and water strategies. Nature Climate Change, 3, 621-626.

IPCC (2014), Climate Change 2014: Synthesis Report. Contribution of Working Groups I, II and III to the Fifth Assessment Report of the Intergovernmental Panel on Climate Change [Core Writing Team, R.K. Pachauri and L.A. Meyer (eds.)]. 151 pp, Geneva, Switzerland.

Jasinski, M.F., & Crago, R.D. (1999). Estimation of vegetation aerodynamic roughness of natural regions using frontal area density determined from satellite imagery. Agricultural and Forest Meteorology, 94, 65-77

Lee, X., Goulden, M.L., Hollinger, D.Y., Barr, A., Black, T.A., Bohrer, G., Bracho, R., Drake, B., Goldstein, A., Gu, L., Katul, G., Kolb, T., Law, B.E., Margolis, H., Meyers, T., Monson, R., Munger, W., Oren, R., Paw, U.K., Richardson, A.D., Schmid, H.P., Staebler, R., Wofsy, S., & Zhao, L. (2011). Observed increase in local cooling effect of deforestation at higher latitudes. Nature, 479, 384-387

Li, H., Li, Y., Wang, T., Wang, Z.H., Gao, M., & Shen, H. (2021). Quantifying 3D building form effects on urban land surface temperature and modeling seasonal correlation patterns. Building and Environment, 204

Li, H., Liu, Y., Zhang, H., Xue, B., & Li, W. (2021). Urban morphology in China: Dataset development and spatial pattern characterization. Sustainable Cities and Society, 71, 102981

Li, J., Song, C., Cao, L., Zhu, F., Meng, X., & Wu, J. (2011). Impacts of landscape structure on surface urban heat islands: A case study of Shanghai, China. Remote Sensing of Environment, 115, 3249-3263

Li, P., Xu, T., Wei, S., & Wang, Z.H. (2022). Multi-objective optimization of urban environmental system design using machine learning. Computers, Environment and Urban Systems, 94, 101796

Li, Y., Schubert, S., Kropp, J.P., & Rybski, D. (2020). On the influence of density and morphology on the Urban Heat Island intensity. Nature Communication, 11, 2647

Li, Z., & Hu, D. (2022). Exploring the relationship between the 2D/3D architectural morphology and urban land surface temperature based on a boosted regression tree: A case study of Beijing, China. Sustainable Cities and Socie ty, 78, 103392

Lu, H., Li, F., Yang, G., & Sun, W. (2021). Multi-scale impacts of 2D/3D urban building pattern

in intra-annual thermal environment of Hangzhou, China. International Journal of Applied Earth Observation and Geoinformation, 104

Manoli, G., Fatichi, S., Bou-Zeid, E., & Katul, G.G. (2020). Seasonal hysteresis of surface urban heat islands. Proceedings of the National Academy of Sciences of the United States of America, 117, 7082-7089

Martinez-Bravo, M.D., Martinez-del-Rio, J., & Antolin-Lopez, R. (2019). Trade-offs among urban sustainability, pollution and livability in European cities. Journal of Cleaner Production, 224, 651-660

Masek, J.G., Wulder, M.A., Markham, B., McCorkel, J., Crawford, C.J., Storey, J., & Jenstrom, D.T. (2020). Landsat 9: Empowering open science and applications through continuity. Remote Sensing of Environment, 248

Meier, R., Davin, E.L., Bonan, G.B., Lawrence, D.M., Hu, X., Duveiller, G., Prigent, C., & Seneviratne, S.I. (2022). Impacts of a revised surface roughness parameterization in the Community Land Model 5.1. Geoscientific Model Development, 15, 2365-2393

Mirzaei, P.A., & Haghighat, F. (2010). Approaches to study Urban Heat Island – Abilities and limitations. Building and Environment, 45, 2192-2201

Moriwaki, R., Kawai, T., Kanega, M., Kanda, M., & Sugawara, H. (2007). Roughness Lengths for Momentum and Heat Derived from Outdoor Urban Scale Models. Journal of Applied Meteorology and Climatology, 46, 1067-1079

Myint, S.W., Zheng, B., Talen, E., Fan, C., Kaplan, S., Middel, A., Smith, M., Huang, H.-p., & Brazel, A. (2017). Does the spatial arrangement of urban landscape matter? examples of urban warming and cooling in phoenix and las vegas. Ecosystem Health and Sustainability, 1, 1-15

Nakai, T., Sumida, A., Daikoku, K.i., Matsumoto, K., van der Molen, M.K., Kodama, Y., Kononov, A.V., Maximov, T.C., Dolman, A.J., Yabuki, H., Hara, T., & Ohta, T. (2008). Parameterisation of aerodynamic roughness over boreal, cool- and warm-temperate forests. Agricultural and Forest Meteorology, 148, 1916-1925

Oke, T.R. (1973). City size and the urban heat island. Atmospheric Environment (1967), 7, 769-779

Oke, T.R. (1976). The distinction between canopy and boundary-layer urban heat islands. Atmosphere, 14, 268-277.

Peng, J., Jia, J., Liu, Y., Li, H., & Wu, J. (2018). Seasonal contrast of the dominant factors for spatial distribution of land surface temperature in urban areas. Remote Sensing of Environment, 215, 255-267

Peng, J., Xie, P., Liu, Y., & Ma, J. (2016). Urban thermal environment dynamics and associated landscape pattern factors: A case study in the Beijing metropolitan region. Remote Sensing of Environment, 173, 145-155

Peng, S., Piao, S., Ciais, P., Friedlingstein, P., Ottle, C., Breon, F.M., Nan, H., Zhou, L., & Myneni, R.B. (2012). Surface urban heat island across 419 global big cities. Environmental Science & Technology, 46, 696-703

Raupach, M. (1994). Simplified expressions for vegetation roughness length and zero-plane displacement as functions of canopy height and area index. Boundary-Layer Meteorology, 71, 211-216

Rotach, M. W. (1994). Determination of the zero plane displacement in an urban environment. Boundary-Layer Meteorology, 67(1), 187-193

Schaudt, K., & Dickinson, R. (2000). An approach to deriving roughness length and zero-plane

displacement height from satellite data, prototyped with BOREAS data. Agricultural and Forest Meteorology, 104, 143-155

Skamarock, W. C., & Klemp, J. B. (2008). A time-split nonhydrostatic atmospheric model for weather research and forecasting applications. Journal of Computational Physics, 227(7), 3465-3485

Song, J., & Wang, Z.H. (2015). Interfacing urban land-atmosphere through coupled urban canopy and atmospheric models. Boundary-Layer Meteorology, 154(3), 427-448

Song, J., & Wang, Z.H. (2016). Evaluating the impact of built environment characteristics on urban boundary layer dynamics using an advanced stochastic approach. Atmospheric Chemistry and Physics, 16, 6285-6301

Sud, Y., Shukla, J., & Mintz, Y. (1988). Influence of land surface roughness on atmospheric circulation and precipitation: A sensitivity study with a general circulation model. Journal of Applied Meteorology and Climatology, 27, 1036-1054

Sulla-Menashe, D., & Friedl, M.A. (2018). User guide to collection 6 MODIS land cover (MCD12Q1 and MCD12C1) product. USGS: Reston, VA, USA, 1-18

Sun, T., Wang, Z.H., & Ni, G. (2013). Revisiting the hysteresis effect in surface energy budgets. Geophysical Research Letters, 40, 1741-1747

Sun, J., & Li, T. (2018). Relationship of Lane Width to Speed for Urban Expressway: A Case Study in Shanghai. In, 2018 International Conference on Network, Communication, Computer Engineering (NCCE 2018) (pp. 1-6): Atlantis Press

Tian, X., Li, Z.Y., van der Tol, C., Su, Z., Li, X., He, Q.S., Bao, Y.F., Chen, E.X., & Li, L.H. (2011). Estimating zero-plane displacement height and aerodynamic roughness length using synthesis of LiDAR and SPOT-5 data. Remote Sensing of Environment, 115, 2330-

2341

United Nations (UN) (2019), World Urbanization Prospects: The 2018 Revision, 126 pp, The United Nations' Department of Economic and Social Affairs - Population Division, New York.

Voogt, J.A., & Oke, T.R. (2003). Thermal remote sensing of urban climates. Remote Sensing of Environment, 86, 370-384

Wang, C., Wang, Z.H., & Yang, J. (2018). Cooling effect or urban trees on the built environment of contiguous United States. Earth's Future, 6, 1066-1081.

Wang, C., Wang, Z.H., & Yang, J. (2019a). Urban water capacity: Irrigation for heat mitigation. Computers, Environment and Urban Systems, 78, 101397

Wang, C., Wang, Z.H., Wang, C., & Myint, S.W. (2019b). Environmental cooling provided by urban trees under extreme heat and cold waves. Remote Sensing of Environment, 227, 28-43

Wan, Z. (2014). New refinements and validation of the collection-6 MODIS land-surface temperature/emissivity product. Remote Sensing of Environment, 140, 36-45

Wang, Z.H. (2014a). Monte Carlo simulations of radiative heat exchange in a street canyon with trees. Solar Energy, 110, 704-713

Wang, Z.H. (2014b). A new perspective of urban-rural differences: The impact of soil water advection. Urban Climate, 10, 19-34

Wang, Z.H. (2021). Compound environmental impact of urban mitigation strategies: Co-benefits, trade-offs, and unintended consequence. Sustainable Cities and Society, 75, 103284

Wang, Z.H. (2022). Reconceptualizing urban heat island: Beyond the urban-rural dichotomy.

Sustainable Cities and Society, 77, 103581

Wang, Z.H., Bou-Zeid, E., Au, S.K., & Smith, J.A. (2011). Analyzing the sensitivity of WRF's single-layer urban canopy model to parameter uncertainty using advanced Monte Carlo simulation. Journal of Applied Meteorology and Climatology, 50(9), 1795-1814

Wang, Z.H., Bou‐Zeid, E., & Smith, J.A. (2013). A coupled energy transport and hydrological model for urban canopies evaluated using a wireless sensor network. Quarterly Journal of the Royal Meteorological Society, 139(675), 1643-1657

Yang, J., Yang, Y., Sun, D., Jin, C., & Xiao, X. (2021). Influence of urban morphological characteristics on thermal environment. Sustainable Cities and Society, 72, 103045

Yang, R., & Friedl, M.A. (2003). Determination of roughness lengths for heat and momentum over boreal forests. Boundary-Layer Meteorology, 107, 581-603

Yuan, B., Zhou, L., Dang, X., Sun, D., Hu, F., & Mu, H. (2021). Separate and combined effects of 3D building features and urban green space on land surface temperature. Journal of Environmental Management, 295, 113116

Yuan, F., & Bauer, M.E. (2007). Comparison of impervious surface area and normalized difference vegetation index as indicators of surface urban heat island effects in Landsat imagery. Remote Sensing of Environment, 106(3), 375-386

Zha, Y., Gao, J., & Ni, S. (2003). Use of normalized difference built-up index in automatically mapping urban areas from TM imagery. International Journal of Remote Sensing, 24, 583-594

Zhao, L., Lee, X., Smith, R.B., & Oleson, K. (2014). Strong contributions of local background climate to urban heat islands. Nature, 511, 216-219

Zhang, J., Li, Z., & Hu, D. (2022). Effects of urban morphology on thermal comfort at the micro-

scale. Sustainable Cities and Society, 86, 104150

Zhou, B., Rybski, D., & Kropp, J.P. (2013). On the statistics of urban heat island intensity. Geophysical Research Letters, 40, 5486-5491

Zhou, D., Zhao, S., Liu, S., Zhang, L., & Zhu, C. (2014). Surface urban heat island in China's 32 major cities: Spatial patterns and drivers. Remote Sensing of Environment, 152, 51-61